

Multiscale and Multiphysics Solvers for AlGaAs TJ-VCSEL

Original

Multiscale and Multiphysics Solvers for AlGaAs TJ-VCSEL / Gullino, Alberto; Tibaldi, Alberto; Bertazzi, Francesco; Goano, Michele; Debernardi, Pierluigi. - STAMPA. - 1005:(2023), pp. 190-195. (Intervento presentato al convegno 53rd Annual Meeting of the Italian Electronics Society tenutosi a Pizzo Calabro nel 7-9 Settembre 2022) [10.1007/978-3-031-26066-7_30].

Availability:

This version is available at: 11583/2976615 since: 2023-03-06T13:06:34Z

Publisher:

Springer

Published

DOI:10.1007/978-3-031-26066-7_30

Terms of use:

This article is made available under terms and conditions as specified in the corresponding bibliographic description in the repository

Publisher copyright

Springer postprint/Author's Accepted Manuscript

This version of the article has been accepted for publication, after peer review (when applicable) and is subject to Springer Nature's AM terms of use, but is not the Version of Record and does not reflect post-acceptance improvements, or any corrections. The Version of Record is available online at: http://dx.doi.org/10.1007/978-3-031-26066-7_30

(Article begins on next page)

Multiscale and multiphysics solvers for AlGaAs TJ-VCSEL

Alberto Gullino¹[0000–0003–1570–0328], Alberto Tibaldi^{1,2}[0000–0002–0157–8512],
Francesco Bertazzi^{1,2}[0000–0002–9409–4807], Michele
Goano^{1,2}[0000–0003–2870–1549], and Pierluigi Debernardi²[0000–0003–1776–3170]

¹ Dipartimento di Elettronica e Telecomunicazioni, Politecnico di Torino,
Corso Duca degli Abruzzi 24, 10129 Torino, Italy

² CNR-IEIT, Corso Duca degli Abruzzi 24, 10129 Torino, Italy
alberto.gullino@polito.it

Abstract. Among possible strategies to improve the performance of vertical-cavity surface-emitting lasers (VCSELs) for short-reach interconnects, current injection schemes based on tunnel junctions (TJs) may be an enabling technology to meet the high temperature requirements of data-center applications. Although TJs have been widely used in different applications, their use in near infrared AlGaAs/GaAs VCSELs has so far received less attention. To assess the merits of TJs in this context, we perform a comparative simulation-based study of a commercial *pin* VCSEL and a modified structure where holes are injected into the active region through a TJ. Band-to-band tunneling probabilities are computed within a multiband nonequilibrium Green’s function (NEGF) approach. The resulting generation rates are included in a quantum-corrected drift-diffusion model for carrier transport. The optical modes of the cavity are found with an electromagnetic solver, and self-heating effects are studied with a thermal model. The comparative multiphysical 1D and 3D simulations of *pin* and TJ-VCSELs predict that the voltage penalty introduced by the reverse-biased TJ is largely compensated by the higher output optical power.

Keywords: VCSEL · Optoelectronics · Physics-based · NEGF · TJ

1 Introduction

The staggering growth of intra-datacenter data traffic demands the improvement of state-of-the-art AlGaAs/GaAs 850 and 980 nm vertical-cavity surface-emitting lasers (VCSELs) performance, crucial for efficient and fast short-reach interconnects [1–4]. Low production costs, array-oriented manufacturability, and small power consumption determine the market dominance of VCSELs as reliable optical sources for on-chip communication. However, data centers represent harsh environments for VCSELs, as server racks reach temperatures up to 85 °C [5].

At present, the commercial near-IR lasers are based on AlGaAs *pin* devices, with an intrinsic active region including some quantum wells (QW) embedded between two oppositely doped semiconductor distributed Bragg’s reflectors

(DBRs). The p -doped top mirror (DBR) introduces higher free-carrier absorption (FCA) losses and larger electrical resistivity with respect to the n -doped counterparts. This causes an earlier thermal roll-over due to self-heating, and a worse RC time constant, that limits the VCSEL bandwidth.

An alternative VCSEL design relies on the introduction of tunnel junctions (TJs) to obtain current injection inside the active region and limit lossy p -doped region to just few nanometers of the TJ. A TJ is a heavily doped pn junction working in reverse bias conditions where purely quantum direct band-to-band tunneling (BTBT) mechanism dominates transport. Lithographically defined TJs are already implemented in short and mid-IR VCSELs [6–9] where it is not possible to grow any oxide aperture; furthermore, TJs are used in GaN/AlGaIn light emitting diodes, to reduce at minimum the p -doping that is characterized by very large acceptor ionization energies [10, 11]. In AlGaAs system, TJs were first introduced by Prof. Ebeling’s group [12, 13].

However, the market pervasion of the pin VCSELs suggests that a technologically computer aided design (TCAD) approach should be preferred to avoid slow and expensive try-and-error prototyping campaigns. In this perspective, accurate and efficient physics-based tools should be developed. Therefore, here we follow the procedure presented in [14]: the same set of fitting parameters is used to calibrate our reduced dimensionality solver D1ANA to reproduce the results on a test TJ-VCSEL, characterized with our in-house multiphysics and multiscale solver VENUS [15–17]. In this way, we have a very accurate but time-consuming solver, and a faster solver that provides reasonable predictions of TJ-VCSEL characteristics, and therefore is suited for extended parametric campaigns.

Further details about the VENUS and D1ANA will be provided in the next section. The structures are described in details in the third section. The results from VENUS and D1ANA are presented in the fourth section.

2 Adopted methodology

The complexity of VCSELs operation requires a multiscale and multiphysics approach. The electrical, optical and thermal problems must be investigated in a comprehensive self-consistent scheme. In this view, our group developed VENUS, a physics-based in-house 3D software able to describe accurately the operation of commercial pin VCSELs, as demonstrated in [15, 16].

VENUS consists in three main building blocks. The electrical transport problem is treated by means of a quantum-correct drift-diffusion model (DD). Quantum corrections describe quantization effects in the nanostructured active region, needed to determine the optical gain/absorption features. The bound states are computed by solving a multiband k -p Schrödinger equation; gain is computed with the Fermi’s golden rule [18]. A capture/escape GR rate is introduced alongside other processes such as Auger and SRH recombinations to connect 2D and 3D population, thus ensuring carrier balance. Carriers in the QWs are described with an additional set of continuity equations. The optical problem is solved through our in-house electromagnetic solver VELM [19, 20]. The optical modes

are retrieved by imposing the resonance condition after a full round-trip. The corresponding eigenvalue problem is solved, returning the resonance wavelength and the modal losses. The computed eigenvectors represent the field expansion coefficients used to compute the optical field. This is used to extract a stimulated rate emission rate, connecting the optical and electrical problems. Eventually, the temperature variation due to self-heating processes (FCA, Joule, non-radiative and radiative transitions) is computed by solving the static heat equation.

The modeling of the TJ cannot be demanded to a semiclassical drift-diffusion model. BTBT is a purely quantum mechanical phenomenon that must be tackled with a genuine quantum approach. Therefore, the tunneling across the TJ is computed with a nonequilibrium Green's function (NEGF) model based on the same electronic structure model used to compute the QW gain. NEGF extracts the interband spectral current by introducing fully nonlocal scattering self-energies computed in the self-consistent Born approximation (SCBA) [21–23]. By integrating such a spectral current over the conduction or the valence band, a current density J_{TJ} is retrieved. From the latter, a generation rate G_{BTBT} is computed and inserted in the DD alongside the other GR mechanisms.

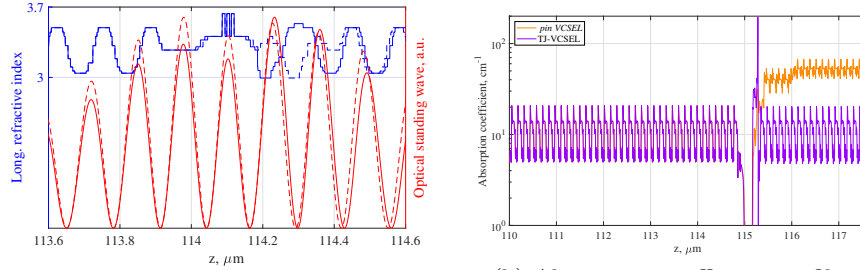
However, the computational burden entailed by a 3D simulation limits the use of VENUS in extended parametric campaigns. Therefore, a reduced dimensionality (1D) solver called D1ANA is derived from VENUS. All the building blocks of the VENUS are converted into their 1D form and applied to a vertical cut taken from the center of the axisymmetric 3D structure. The steps required to calibrate D1ANA to reproduce the experimental results on the commercial *pin* VCSEL are discussed in depth in [14].

3 Investigated structure

The test TJ-VCSEL is generated starting from a commercial *pin* VCSEL. The structure described in depth in [14–16]: here we report some details for the reader convenience. The active region embeds three 8 nm GaAs QWs in a 1λ -cavity. The bottom *n*-DBR is realized with 37 pairs with Al molar fraction concentration varying from 17% to 90%; the top outcoupling *p*-DBR is composed of 21 pairs with the same concentrations. The 30 nm thick oxide aperture with diameter $4.7\mu\text{m}$ is placed in the first node of the optical standing wave (SW) to reduce the current threshold [24]. This provides both optical and electrical lateral confinement. The top metallic contact consists of a metal ring (inner radius $6\mu\text{m}$) deposited on the topmost GaAs layer, where an ohmic contact is realized with a heavily *p*-doped GaAs layer, which is afterwards etched by 60 nm after the contact ring is defined.

The test TJ-VCSEL is realized by placing the TJ in the same position of the oxide aperture (see Fig. 1a), to reduce the impact of the strong doping levels on the FCA losses of the structure. The *n*-side is doped with tellurium, with density $N_D = 3 \cdot 10^{19} \text{ cm}^{-3}$; the *p*-side is doped with carbon, with density of $N_A = 2 \cdot 10^{20} \text{ cm}^{-3}$, and we assume an abrupt doping profile. Dopants diffusion impact in the TJ operation will be investigated in future papers. The TJ is

extended across the whole VCSEL mesa; lateral confinement is demanded to the oxide aperture. As the SW node is occupied by the TJ, in our test structure the oxide is placed in an intermediate position, between a node and an antinode of the SW. Different configurations will be investigated in future works. The presence of the TJ allows to switch the top mirror into a n -doped DBR. The consequent reduction of FCA losses (see Fig. 1b) allows to reduce the number of the outcoupling mirror pairs by two, to match the threshold gain of the *pin* VCSEL.



(a) Refractive index profiles and corresponding SW. Dashed lines: *pin* VCSEL; solid lines: TJ-VCSEL.

(b) Absorption coefficient profiles.

Fig. 1: (a) shows the different absorption coefficient levels: in the TJ-VCSEL there is a strong absorption in the TJ region, whereas in the top DBR (right mirror) it is greatly reduced. In (b), the refractive index and the corresponding SW are reported for the two structures. The QWs are aligned, but the introduction of the TJ shifts the position of the oxide aperture in the TJ-VCSEL.

4 Results

In this section the results on the TJ-VCSEL are compared to the commercial *pin* device. These are obtained with VENUS and the calibrated D1ANA, starting with the same set of parameters used in [14]. In summary, they are: thermal conductivity and its temperature dependence, refractive index profile as a function of temperature dn/dT , carrier mobilities, and effective size of the oxide aperture.

In Fig. 2, the static figure of merits of the two VCSELs are reported. The curves in purple represent the result of the calibration process realized in [14]. In Fig. 2a, D1ANA underestimates the current with respect to experimental and VENUS data at high bias levels. This is related to the current crowding effect in the oxide aperture proximity, and to the current flowing radially from the top annular contact, both neglected in a 1D framework. On the other hand, in Fig. 2b, D1ANA is more reliable in predicting the output optical power, and well reproduces the 3D results.

Moving to the TJ-VCSEL case (orange curves), the results remain consistent if two of the aforementioned parameters are further adjusted with respect to the *pin* case. In particular, the thermal dependence introduced on carrier mobilities and dn/dT are reduced. In Fig. 2a, there is the same issue encountered in the *pin* case at high applied bias, despite the mentioned mobility reduction. However, a remarkable difference arises at low bias, where D1ANA predicts larger values of current than VENUS. The discrepancy could be explained by the presence of the TJ, that is not radially limited. While the oxide aperture introduces the current crowding, that increases the density of current, conversely the TJ forces a large radial current, that could reduce current density, but is not predicted by D1ANA. In Fig. 2b, the optical characteristics are reported. As in the commercial VCSEL case, D1ANA reproduces the main features of the experimental curve, such as the threshold current at ≈ 0.5 mA, the maximum output power of 4.5 mW at a current of 10 mA.

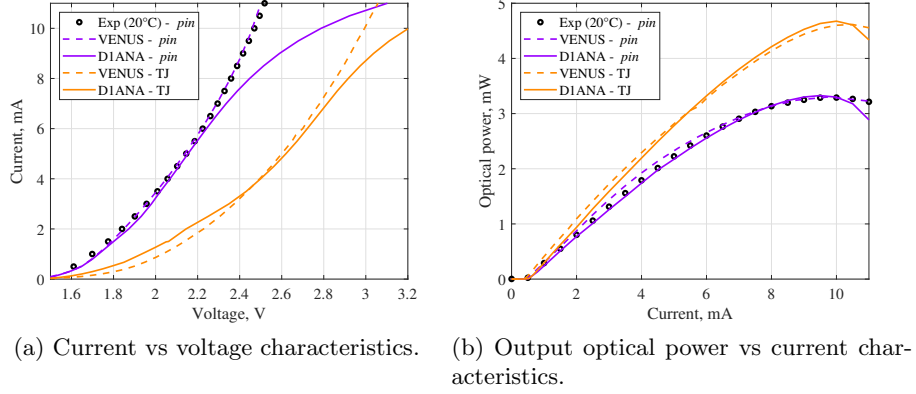


Fig. 2: Static characteristics of *pin* and TJ-VCSELs (purple and orange curves, respectively), computed with VENUS (dashed) and D1ANA (solid curves).

In Fig. 3, the emission wavelength is displayed as a function of the driving current. This figure of merit is useful to evaluate the VCSEL red-shift, caused by self-heating, and therefore the inner temperature variation. The results from VENUS (dashed curves) are superimposed for the two structures, close to the experimental data. D1ANA provides good predictions on both the VCSELs. However, the dn/dT factor is reduced in the TJ-VCSEL case.

The variation of the two fitting parameters entails that in TJ-VCSEL the temperature rises more than in the *pin* structure. This appears to be in contrast with the prediction of a reduced self-heating induced by the *n*-doped DBR. However, TJ-VCSEL enables larger optical power, that in turn increase both the radiative and FCA losses, that play a main role in the self-heating process.

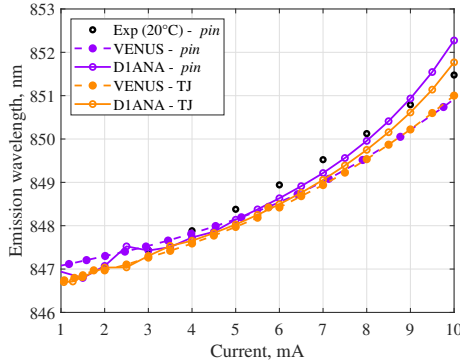


Fig. 3: Emission wavelength as a function of current flowing into the *pin* and TJ-VCSEL (purple and orange curves, respectively), computed with VENUS (dashed) and D1ANA (solid curves).

5 Conclusions

We have demonstrated that our calibrated one-dimensional solver is able to reproduce the main static characteristics of a TJ-VCSEL, within a NEGF-DD model. The electrical characteristics show that the presence of the TJ causes an electrical penalty with respect to the *pin* device, related to the additional junction. At the same time, the TJ-VCSEL improves the output optical power at equal current values. The increased slope of the curve is induced by the out-coupling losses reduction, leading to a larger maximum optical power. Thermal roll-over makes the two VCSELs turn off at similar currents.

References

1. J. A. Tatum, *et al.*, *J. Lightwave Technol.* **33**, 727 (2015).
2. N. Ledentsov Jr., M. Agustin, L. Chorchos, N. N. Ledentsov, J. P. Turkiewicz, *Electron. Lett.* **54**, 774 (2018).
3. G. Kanakis, *et al.*, *MDPI Appl. Sci.* **9** (2019).
4. A. Larsson, *et al.*, *2020 IEEE Photonics Conference (IPC)* (2020), pp. 1–2.
5. P. Westbergh, J. S. Gustavsson, A. Larsson, *Optical Fiber Communication Conference* (Optical Society of America, 2015), p. M2D.5.
6. M. Ortsiefer, *et al.*, *Japan. J. Appl. Phys.* **39**, 1727 (2000).
7. W. Hofmann, M. Muller, G. Bohm, M. Ortsiefer, M.-C. Amann, *IEEE Photon. Technol. Lett.* **21**, 923 (2009).
8. A. Bachmann, K. Kashani-Shirazi, S. Arafin, M.-C. Amann, *IEEE J. Select. Topics Quantum Electron.* **15**, 933 (2009).
9. G. K. Veerabathran, S. Sprengel, A. Andrejew, M.-C. Amann, *Appl. Phys. Lett.* **110**, 071104 (2017).
10. J. T. Leonard, *et al.*, *Appl. Phys. Lett.* **107**, 091105 (2015).
11. M. Žak, *et al.*, *Phys. Rev. Appl.* **15**, 024046 (2021).

12. T. Knödl, M. Golling, A. Straub, K. J. Ebeling, *Electron. Lett.* **37**, 31 (2001).
13. T. Knödl, *et al.*, *IEEE J. Select. Topics Quantum Electron.* **9**, 1406 (2003).
14. A. Gullino, A. Tibaldi, F. Bertazzi, M. Goano, P. Debernardi, *MDPI Appl. Sci.* **11**, 6908 (2021).
15. A. Tibaldi, F. Bertazzi, M. Goano, R. Michalzik, P. Debernardi, *IEEE J. Select. Topics Quantum Electron.* **25**, 1500212 (2019).
16. P. Debernardi, *et al.*, *IEEE J. Select. Topics Quantum Electron.* **25**, 1700914 (2019).
17. A. Tibaldi, *et al.*, *Opt. Quantum Electron.* **51**, 231 (2019).
18. S. L. Chuang, *Physics of Photonic Devices* (John Wiley & Sons, Hoboken, 2009).
19. P. Debernardi, *IEEE J. Quantum Electron.* **45**, 979 (2009).
20. P. Debernardi, *et al.*, *IEEE J. Select. Topics Quantum Electron.* **28**, 1700111 (2022).
21. A. Tibaldi, *et al.*, *Phys. Rev. Appl.* **14**, 024037 (2020).
22. A. Tibaldi, *et al.*, *20th International Conference on Numerical Simulation of Optoelectronic Devices (NUSOD 2020)* (online, 2020), pp. 67–68.
23. A. Gullino, *et al.*, *21st International Conference on Numerical Simulation of Optoelectronic Devices (NUSOD 2021)* (online, 2021), pp. 79–80.
24. B. Demeulenaere, P. Bienstman, B. Dhoedt, R. Baets, *IEEE Journal of Quantum Electronics* **35**, 358 (1999).